Mass changes of the northern Antarctic Peninsula Ice Sheet derived from repeat bi-static SAR acquisitions for the period 2013-2017

Thorsten C. Seehaus[1], Christian Sommer[1], Thomas Dethinne[2,3], Philipp Malz[1]

[1]Institute of Geography, Friedrich-Alexander-Universität Erlangen-Nürnberg, 91058 Erlangen, Germany
5   [2]Laboratory of Climatology, University of Liège, Liège, Belgium
[3]Centre Spatial de Liège, University of Liège, Liège, Belgium

Correspondence to: Thorsten C. Seehaus (thorsten.seehaus@fau.de)

Abstract. Some of the highest specific mass change rates in Antarctica are reported for the Antarctic Peninsula. However, the existing estimates for the northern Antarctic Peninsula (<70°S) are either spatially limited or are affected by considerable
10   uncertainties. The complex topography, frequent cloud cover, limitations in ice thickness information, boundary effects, and uncertain glacial-isostatic adjustment estimates affect the ice sheet mass change estimates using altimetry, gravimetry, or the input-output method. Within this study, the first assessment of the geodetic mass balance throughout the ice sheet of the northern Antarctic Peninsula is carried out employing bi-static SAR data from the TanDEM-X satellite mission. Repeat coverages from austral-winters 2013 and 2017 are employed. An overall coverage of 96.4% of the study area by surface
15   elevation change measurements and a total mass budget of -24.1±2.8 Gt/a is revealed. The spatial distribution of the surface elevation and mass changes points out, that the former ice shelf tributary glaciers of the Prince-Gustav-Channel, Larsen-A&B, and Wordie ice shelves are the hotpots of ice loss in the study area, and highlights the long-lasting dynamic glacier adjustments after the ice shelf break-up events. The highest mass change rate is revealed for the Airy-Seller-Fleming glacier system of -4.9±0.6 Gt/a and the highest average surface elevation change rate of -2.30±0.03 m/a is observed at Drygalski
20   Glacier. The comparison of the ice mass budget with anomalies in the climatic mass balance indicates, that for wide parts of the southern section of the study area the mass changes can be partly attributed to changes in the climatic mass balance. However, imbalanced high ice discharge drives the overall ice loss. The previously reported connection between mid-ocean warming along the southern section of the west coast and increased frontal glacier recession does not repeat in the pattern of the observed glacier mass losses, excluding Wordie Bay. The obtained results provide information on ice surface elevation
25   and mass changes for the entire northern Antarctic Peninsula on unprecedented spatially detailed scales and high precision, and will be beneficial for subsequent analysis and modelling.

1 Introduction and study area

The ice sheet of the Antarctic Peninsula (AP) is strongly affected by the changing climate conditions (e.g. IMBIE Team, 2018; Scambos et al., 2014). A pronounced rise in the air temperature along the AP was reported in the 20th century (Turner
30   et al., 2016). However, since the turn of the millennia a cooling trend was observed (Oliva et al., 2017; Turner et al., 2016).

Recent analysis suggests an end of the intermediate cooling and the return of a temperature increase (Carrasco et al., 2021). The record summer temperatures measured at stations on the northern AP in the last years are in line with this finding.

Large parts of the coastline of the AP are surrounded by ice shelves, buttressing the ice discharge of the tributary glaciers. Between the 1950s and 2010s, about 28.000 km² of the ice shelf area was lost (Cook and Vaughan, 2010). Most notable are the disintegration of ice shelves, like Larsen-A and Prince Gustav ice shelves in 1995, Larsen-B Ice Shelf in 2002, and the recession of Wordie Ice Shelf since the 1960s (Wendt et al., 2010). As a consequence, the former tributary glaciers reacted by further frontal retreat, increased flow speeds, and ice mass loss due to the loss of the frontal buttressing (e.g. Friedl et al., 2018; Rott et al., 2011; Scambos, 2004; Seehaus et al., 2015; Wuite et al., 2015). Various studies suggest that the atmospheric warming on the AP in the 20th century has triggered these events (Scambos et al., 2003; Turner et al., 2016; Vaughan et al., 2003). Moreover, higher basal melt rate caused by warming ocean water might have thinned and weakened the ice shelves before their collapses, as predicted for Larsen C Ice Shelf (Hogg and Gudmundsson, 2017; Holland et al., 2015). Another phenomenon affecting the AP ice sheet is the up-welling of warm Circumpolar Deep Water (CDW) along the south-west coast of the AP (Holland et al., 2010), potentially leading to increased subaqueous melt, frontal recession, and ice discharge (Cook et al., 2016; Hogg et al., 2017; Walker and Gardner, 2017; Wouters et al., 2015).

These different processes are the main drivers of the observed increase in ice mass loss on the AP from 7±13 Gt/a in the period 1992-1997 to 33±16 Gt/a in the period 2012-2017 (IMBIE Team, 2018). Even though, the analysis by the Ice Sheet Mass Balance Inter-comparison Exercise (IMBIE) team relies on mass balance estimates from various methods (altimetry, gravimetry, input-output methods), the reported values are affected by considerable uncertainties. The mean mass budget estimates of the different methods have uncertainties of up to 90% and differ by up to 500%. Frequent cloud cover and the complex topography along the AP, especially in the regions north of 70°S, imply limitations for altimetric measurements (Schröder et al., 2019; Shepherd et al., 2019). The gravimetric glacier mass budget estimates stretch from -39 to -9 Gt/a with uncertainties in the range of 1-24 Gt/a (IMBIE Team, 2018). These limitations can be attributed to the small West to East extent of the AP, mass changes on the surrounding island as well as uncertain regional glacial-isostatic adjustment (GIA) estimates of the Earth crust (Horwath and Dietrich, 2009). Within the overlap period (2002-2010), both input-output method-based mass balances estimates for the AP, employed by the IMBIE assessment, differ by up to 30 Gt/a, which is comparable to the mean mass budget in the period 2012-2017. The uncertainty of the input-output method is mainly caused by the uncertainty of the modelled climatic mass balance (CMB) and the accuracy of the available ice thickness data, which has certain limitations on the AP (Seehaus et al., 2015), used to compute the ice flux (IMBIE Team, 2018).

Studies on regional and mountain range scales (Abdel Jaber et al., 2019; Malz et al., 2018, Seehaus et al. 2020) as well as on continental to global scale (Braun et al., 2019; Brun et al., 2017; Dussaillant et al., 2019; Hugonet et al. 2021) highlighted the suitability and accuracy of the geodetic method. There is currently no geodetic mass balance estimation covering large regions of the AP, like the drainage basins defined by Rignot et al. (2011) or Zwally et al. (2012). Scambos et al. (2014) provided the most extended geodetic mass balance computation on the AP, partially covering regions north of 66°S for the primarily period 2003-2008. The authors used SPOT5 and ASTER stereo imagery, in combination with ICESat-1 altimeter

65   data. Due to the frequent cloud cover on the AP, analyses based on optical satellite data are less suitable due to limited coverage (Dussaillant et al., 2019; Hugonet et al., 2021). Whereas analyses based on interferometric SAR data (e.g. Malz et al., 2018; Seehaus et al., 2019) are not limited by the weather conditions. Since 2011, the bistatic Synthetic Aperture Radar (SAR) satellite mission TanDEM-X (TDX) has been acquiring data along the AP. Several complete coverages of the AP were acquired for the "global DEM" and "change DEM" missions of TanDEM-X. Various studies showed the feasibility of

70   obtaining geodetic mass balances on the AP on glacier and multi-glacier scales (Rott et al., 2018, 2014; Seehaus et al., 2015, 2016). Consequently, this study aims to carry out the first large-scale geodetic mass balance analysis on the AP based on TDX data.

    The study area is limited to the AP Ice Sheet north of 70°S, excluding the surrounding islands (see Figure 1). This spatial extend was selected, since (1) this section of the AP is strongly affected by the disintegration of ice shelves, (2) up-welling

75   of CDW along the west coast, and (3) limitations of mass budget estimates based on altimetry, gravimetry and input-output method (see above). An area-wide geodetic mass balance assessment based on TanDEM-X data will provide unprecedented spatially detailed and precise analysis, and will be highly spatially complementary to the results based on other approaches for the more southern sections of the AP.

2 Data

80   In order to obtain surface elevation information at the study site, bistatic Synthetic Aperture Radar (SAR) acquisitions from the TanDEM-X mission were used. Several, most partial, TanDEM-X data coverage of the AP exist since 2011. The surface conditions affect the SAR signal penetration depth in snow and ice (Abdullahi et al., 2018; Rott et al., 2021). A seasonal variability of the mean glacier surface height of about 2 m was reported for the north-eastern AP using TDX data (Seehaus et al., 2015, 2016). However, according to Rott et al. (2018) difference in the SAR signal penetration of TDX can be neglected

85   on the AP when comparing data from winter seasons. This assumption is based on comparing elevation changes from repeated TanDEM-X acquisitions and repeated airborne Lidar measurements from NASA's Operation IceBridge. Consequently, we used two coverages of the AP with TDX data acquisitions from austral-winter 2013 and 2017 for our analysis. A list of all individual TDX acquisitions and certain InSAR parameter can be found in the Supplement. A small data gap in the coverage from 2013 (9.6%) was filled by TDX data from austral-winter 2014 (see Figure 2).

90   A reference DEM (refDEM) is needed for the generation of SAR DEMs based on differential interferometry. The recently published high-resolution DEM of the AP (Dong et al., 2021) based on the global TanDEM-X DEM at 12 m spatial resolution is employed. The authors used information from the Reference Elevation Model of Antarctica (REMA) (Howat et al., 2019) to correct residual systematic elevation errors in the global TanDEM-X DEM, and to obtain enhanced surface height data for the AP. The temporal coverage of the Data used to generate the refDEM is comparable to our TDX coverage

95   in 2013. However, no pixel-specific date information is available for the global TanDEM-X DEM and consequently for the refDEM, justifying the need to reprocess a surface elevation model for this time step.

Output from the regional climate model MAR ("Modèle Atmosphérique Régional" in French) covering whole Antarctica is used to obtain information on the CMB. MAR is a polar-oriented climate model mostly used to study the Greenland (Delhasse et al., 2020; Fettweis et al., 2021) and Antarctic ice sheets (Amory et al., 2021; Gilbert and Kittel, 2021). Hydrostatic approximation of primitives equations described in (Gallée and Schayes, 1994) are the basis of the atmosphere dynamics of the model and its radiative transfer scheme is adapted from (Morcrette, 2002). The energy and mass transfer between the atmosphere and soil is handled by the SISVAT module (Soil Ice Snow Vegetation Atmospheric Transfer (De Ridder and Gallée, 1998)). For this study, the version used is MARv3.12, for which improvements have been described in (Lambin et al., 2022). MAR was run over the AP at a 7.5 km spatial resolution and has been set to resolve the first 20 m of the snowpack, divided into 30 layers of varying thickness. The model is forced by the 6-hourly ERA-5 reanalysis (Hersbach et al., 2020) at the lateral boundaries and over the ocean between March 2006 and May 2022 but the data up to 2008 has been discarded as spin-up. The snowpack is initialized from a previous simulation (Kittel et al., 2021). The parametrization and evaluation of the model over the AP are described in (Dethinne et al., 2023).

The average CMB is computed for the period July 2013 until June 2017 and the absolute and relative difference (dCMB) in respect to whole temporal coverage of the MAR data (2008-2022) is computed to obtain information CMB anomalies during the study period.

By dividing the CMB anomalies (dCMB) by the total mass change ($\Delta M/\Delta t$), we define the mass balance ratio MBR. It indicates the contribution of CMB changes on the mass change. Positive values indicate that dCMB and $\Delta M/\Delta t$ are aligned, e.g. decreased CMB and total mass loss, whereas negative values point out contrary alignment, e.g. increased CMB and total mass loss. MBR values close to 1 indicate that the total mass changes can be mainly attributed to changes in CMB

Information on individual glacier outlines, rock outcrops, and regional drainage basin definitions are taken from Silva et al. (2020), Rignot et al., (2011), and Zwally et al. (2012).

3 Methods

The TDX data was ordered in Coregistered Single Look Complex (CoSSC) format. Consecutive acquisitions from the same date and orbit were concatenated to enhance the subsequent SAR processing and coregistration of the products. The differential interferometric SAR processing approach was applied to derive DEMs from the TDX data by means of the refDEM. ~~The advantage of this approach is, that only the elevation difference between the refDEM and the TDX data needs to be unwrapped, leading to fewer phase-unwrapping issues in areas with complex topography like the AP. The resulting TDX raw DEMs need to be coregistered to remove residual horizontal and vertical offsets, in order to generate a smooth DEM mosaic for each time step and to facilitate the comparison of the DEMs from different dates. The iterative coregistration procedure consists of phase-ramp removal operations and 3D-coregistration based on the algorithm of Nuth and Kääb (2011). More details on the SAR processing and the coregistration procedure can be found in Sommer et al. (2022).~~

First a differential interferogram is generated by means of the refDEM as elevation reference. Afterwards, the interferogram is filtered and unwrapped by applying the minimum cost flow algorithm. The phase-to-height sensitivity is computed by means of a simulated differential interferogram derived from the refDEM and the refDEM lowered by 100 m. Subsequently the unwrapped differential interferogram based on the TDX is data is converted to a differential elevation map by applying the derived phase-to-height sensitivity information. Finally, the height information of the refDEM is added to compute absolute heights and the resulting DEM is orthorectified and geocoded. The advantage of this differential interferometric approach is, that only the elevation difference between the refDEM and the TDX data needs to be unwrapped, leading to fewer phase-unwrapping issues in areas with complex topography like the AP.

The resulting TDX raw DEMs need to be coregistered to remove residual horizontal and vertical offsets, in order to generate a smooth DEM mosaic for each time step and to facilitate the comparison of the DEMs from different dates. The iterative coregistration procedure consists of phase-ramp removal operations and 3D-coregistration based on the algorithm of Nuth and Kääb (2011). More details on the SAR processing and the coregistration procedure can be found in Sommer et al. (2022).

In previous studies (e.g. Braun et al., 2019; Malz et al., 2018; Sommer et al., 2022), the applied coregistration procedure was primarily based on the offset estimation between the refDEM and the TDX DEM on stable areas (ice-free land surfaces). At the AP the amount of ice-free areas is very limited. Less than 4% of the surveyed area is not covered by glacier ice according to the rock masks from Silva et al. (2020). Moreover, many of the ice-free areas are situated at steep slopes, where DEMs are typically less reliable (Toutin, 2002), or SAR layover and shadow limit the availability of elevation data in the individual raw TDX DEMs. Since the refDEM was generated based on TDX acquisitions in austral winters 2013 and 2014, it is assumed that the elevation differences between the refDEM and our TDX DEMs in 2013/14 are minimal in most ice-covered areas. In particular, away from the dynamic glacier tongues and low-lying areas, previous studies reported only minor elevation change rates (Scambos et al., 2014; Seehaus et al., 2016). Consequently, the lower sections (<300 m a.s.l.) and dynamic glacier sections, manually defined by means of NASA MEaSUREs ice velocity mosaics (Mouginot et al., 2017), were masked out and the remaining ice-covered areas were included in the coregistration of TDX DEMs from 2013. The difference between the coregistered TDX DEMs and refDEM revealed some areas with remaining systematic elevation differences, e.g. caused by phase-unwrapping issues, in areas selected for coregistration. Those areas were manually inspected and masked out by an iterative process. For the TDX DEMs in 2017, also an iterative procedure of coregistration relative to the refDEM was applied, consisting of DEM differentiating and updating the masks. At later processing steps, potential biases caused by SAR signal penetration difference were observed at high elevated areas (see below), consequently these areas were also excluded in the iterative coregistration process. While doing this iterative masking, systematic elevation offsets were present in the elevation differences between the refDEM and both TDX DEM mosaics in some areas, mainly around the Larsen-B embayment (see Figure 2c&d). The offsets showed some pattern which can be attributed to mosaicking of individual DEM tiles. The pattern does not fit to the outlines of the individual DEMs used to generate the

TDX DEM mosaics in this study. Thus, it is concluded that remaining residual systematic elevation biases in the refDEM caused these offsets. Consequently, the affected areas were masked out during the coregistration process.

165   The resulting coregistered TDX DEM were mosaicked for both time steps and subtracted to obtain elevation change (dh) information. Mosaics consisting of pixel-wise date information were also generated to allow for a precise definition of elevation change rates ($\Delta h/\Delta t$). Subsequently, the ice mass change rates ($\Delta M/\Delta t$) were computed using the Antarctic Ice Sheet basin definitions 25g and 26g from Zwally et al. (2012) and I-Ipp from Rignot et al. (2011). Additionally, the basin delineations were cropped in latitudinal subsets in 1° steps to investigate potential spatial variations. The ice mass changes

170   were also computed for individual glacier basins larger than 20 km², using the most recent glacier outlines in the glacier inventory of Silva et al. (2020), and other local sub-region definitions for comparison with existing studies (Rott et al., 2018; Scambos et al., 2014). Voids in the elevation change field on glacier areas were filled using local hypsometric interpolation for the analysis of the individual glaciers throughout the AP, which is one of the most suitable methods according to (Seehaus et al., 2020b). The global hypsometric interpolation was applied for the analysis on basin and sub-region scales.

175   For all ice volume computations, the rock-outcrop definition from Silva et al. (2020) was applied to mask out ice-free areas in the different ice sheet basins definitions. The ice volume changes were converted to mass changes using a volume-to-mass conversion factor of 900 kg/m³. Since the most dominant ice volume changes are found for the various former ice shelf tributaries (see Figure 1), this scenario is a suitable factor for ice mass changes dominated by ice dynamics (Kääb et al., 2012). The quality of the generated DEMs and elevation change data was evaluated using data form Operation IceBridge and

180   time-stamped REMA (Reference Elevation Model of Antarctica) DEMs. A good agreement between the TanDEM-X data and the independent height information was obtained, indication the suitability of the TanDEM-X data for geodetic glacier mass balance assessments. A detailed description of the analysis and findings can be found in the Supplement.

Based on comparison with lidar measurements and similarities in the backscatter coefficients, ~~According to~~ Rott et al. (2018) concluded that , differences in the SAR signal penetration can be neglected, when comparing TDX DEMs from austral

185   winters on the AP. Even though, solely TDX austral winter data is used in this analysis, some elevation change patterns in upper glacier regions (see Figure 1 and break in slope of the elevation change data in Figure 3) seems to be caused by differences in the SAR signal penetration between the acquisitions. The analysis of the SAR backscatter coefficients and comparison with REMA DEM tiles also support this assumption (see Supplement). These areas are located at elevations above 1800 m a.s.l. covering an area of 12.306 km², corresponding to 16.4% of 25g & 26g drainage basins. In order to

190   correct for these potential offsets, we applied a linear increasing correction of dh for the elevation range from 1800 – 2400 m a.s.l. of up to 2 m, similar to Braun et al. (2019) or Seehaus et al. (2020a), leading to correction of the volume change by - 2.76 km³ and an average elevation change by 0.04 m/a (25g & 26g basins). The upper limit of 2400 m a.s.l. was defined since only two small peaks in the southern part of the study area stretch above this limit. We are comparing X-band to X-band SAR data, in contrast to Braun et al. (2019), who compared X-band to C-band SAR data and applied a variable

195   correction value of up to 5 m. Thus, a reduced maximum correction value of 2 m was selected based on the findings by Seehaus et al. (2015).,

Finally, the ice mass change rate $\Delta M/\Delta t$ is computed by:

$$\frac{\Delta M}{\Delta t} = \rho \left(\int_S \frac{\Delta h}{\Delta t} dS + \frac{V_{pen}}{\Delta t} \right) \quad (1)$$

Where S is the analysed glacier area, V_{pen} the volume change correction to account for differences in SAR signal penetration at higher elevations (see above), and ρ the volume-to-mass conversion factor. The uncertainty of ice mass changes is computed by:

$$\delta_{\Delta M/\Delta t} = \sqrt{\left(\frac{\Delta M}{\Delta t} \right)^2 \left(\left(\frac{\delta_{\Delta h/\Delta t}}{\frac{\Delta h}{\Delta t}} \right)^2 + \left(\frac{\delta_S}{S} \right)^2 + \left(\frac{\delta_\rho}{\rho} \right)^2 \right) + \left(\frac{V_{pen}}{\Delta t} * \rho \right)^2 + \ddot{\iota}\ddot{\iota}} \quad (2)$$

Where $\delta\Delta h/\Delta t$ is the uncertainty of the elevation change measurements and δS is the uncertainty of the glacier outlines. Even though, the ice loss is dominated by ice discharge, we account for uncertainties in the the volume-to-mass conversion factor due to surface processes by applying a $\delta\rho$ of 60 kg/m³, according to Huss (2013).

To account adequately for the SAR signal penetration bias correction in the error budget of the mass changes, a 100% uncertainty of V_{pen} is assumed. V_{int} is the uncertainty caused by the interpolation of $\Delta h/\Delta t$ in areas without $\Delta h/\Delta t$ measurements. It is computed by multiplying the glacier area with interpolated $\Delta h/\Delta t$ values by the uncertainty of $\Delta h/\Delta t$ caused by the interpolation (0.09 m/a and 0.14 m/a for local and global hypsometric interpolation, respectively), which is computed according to Seehaus et al. (2020b).

$\delta\Delta h/\Delta t$ was estimated based on slope-weighted elevation differences on ice-free areas and considering spatial auto-correlation according to Rolstad et al. (2009), using a correlation length of 318 m (Sommer et al., 2022). In order to account for potential local differences in the accuracy of the elevation changes, only ice-free areas within the individual ice sheet drainage basin, including the latitudinal subsets, were considered for the analysis of the different basins. Most individual glacier basins have very limited ice-free areas. Thus, the slope-weighted elevation differences revealed on the study area wide ice-free surfaces were used for the analysis on glacier scales. However, the individual glacier or basin area was used to account for spatial auto-correlation.

Since the ice sheet basin definitions from Zwally et al. (2012) and Rignot et al. (2011) are fixed standard products for mass balance computations in Antarctica, dS was set to zero when using these basin delineations. However, for the analysis of the individual glaciers dS was estimated using the length of the ice-ocean glacier boundaries time a horizontal uncertainty ± 60 m (reliability rating of 1 according to Ferrigno et al. (2006)).

4 Results and Discussion

The revealed surface elevation information covers 96.4% of the glaciated area of the northern AP Ice Sheet (basin definition 25g&26g) and is illustrated in Figure 1. The spatial distribution of the ice surface elevation changes clearly indicates local

hot spots of ice mass losses for some former ice shelf tributaries of the Larsen-A and B, and Wordie ice shelves. This spatial pattern fits also to altimeter-based observations like (Schröder et al., 2019; Shepherd et al., 2019). It is also clearly visible on the glacier scale analysis of the ice mass changes as illustrated in Figure 4. Surface lowering rates of up to -8 m/a and more, as well as glacier-wide mean surface elevation change rates of -0.71±0.01 m/a, -2.30±0.03 m/a, and -1.99±0.05 m/a are found for Airy-Seller-Fleming (ASF), Drygalski, and Hektoria-Green-Evans (HGE) glaciers, respectively, which account for almost 40% of the total mass loss of the study area. The overall highest ΔM/Δt value of -4.9±0.6 Gt/a is found for ASF Glacier, which is the largest glacier (7710 km²) in the study area. The highest average surface lowering rate is observed at Drygalski Glacier. For a few, mainly small, glaciers there are also slight positive mean Δh/Δt values measured. Cook et al. (2016) proposed for the south-western coast of the AP a correlation between frontal retreat and the warming of mid-ocean water layer, due to up-welling of CDW, since the 1990s. Walker and Gardner (2017) as well as Friedl et al. (2018) attributed the recession and increased ice discharge at Wordie bay to the same phenomena. Our results confirm these propositions at Wordie Bay, where high ice losses are measured. However further north, there is a very heterogeneous change pattern revealed on glacier scales (Figure 4). By averaging the ice sheet changes on 1° latitudinal scales (Figure 5 and Table 1) there is also no correlation observed, regarding the warming pattern reported by Cook et al. (2016). There is to note that the differences in the observation periods of this study and by Cook et al. (2016) (1945-2009) might explain the discrepancies. On the other hand, most glaciers along the west coast are situated in fjord-like valleys. Thus, the frontal retreat might not have destabilized the ice discharge. In order to test this hypothesis, further studies on the evolution of the ice flow are needed.

Even though, for section 66-67°S an average slight mass gain, and for section 68-69°S moderate ice loss is found. The comparison of ΔM/Δt with the average CMB and dCMB values (Figure 5) on latitudinal scales does not show a correlation pattern. The dCMB indicates, that the average CMB throughout the study period was lower in the southern and higher in the northern section of the study site in comparison to the long-term average CMB (Figure 5e). The MBR values obtained in this study are illustrated in Figure 5b and listed in Table 1. Negative MBR is revealed for the northern part of the study area, indicating that changes in CMB were not the driver of mass losses. However, for wide parts of the Larsen-C tributaries along the east coast and the southern section of the west coast positive MBRs are revealed, suggesting that the decrease in CMB contributed to the total mass losses, in particular for the section between 67° and 69°S on the west coast. A negative MBR is revealed for section 66-67°S on the west coast. Here, a slight total mass gain and negative dCMB are found. Thus it can be assumed that reduced ice discharge might have compensated the lower CMB and even led to a mass gain. It is noteworthy that the modelled CMB is subject to considerable uncertainties, which can be assumed in the range of 14-17% on the AP (Rignot et al., 2019), and that the revealed ΔM/Δt values have certain error margins as well. Thus, further analysis of the ice dynamics is needed to back up the drawn conclusions on correlations between CMB and ΔM/Δt, which is beyond the scope of this study.

The Imbalance ratio, defined by Scambos et al. (2014) as the mass change divided by the CMB, serves as an indicator for the ice mass imbalance. It is illustrated in Figure 5c and listed in Table 1. Its spatial pattern generally repeats the ΔM/Δt and

MBR pattern and also clearly indicates the continuous high imbalance of the regions affected by the past ice shelf break-up

260   events.

By splitting the study side into subregions based on the glacier front type (see Figure 6), average $\Delta h/\Delta t$ values of -0.317±0.004 m/a, -0.123±0.004 m/a and -0.171±0.006 m/a are found for former ice shelf tributaries, current ice shelf tributaries, and non-ice shelf tributaries, respectively (Table 1). It indicates that the aftermath of the ice shelf breakup events forces increased mass losses of former tributaries even throughout multiple decades, accounting to 67% of the study area

265   wide mass loss.

Along the coastline of the Larsen-A and B and Wordie embayment, higher glacier flow speeds of the former ice shelf tributaries are reported by Rott et al. (2018), Seehaus et al. (2018), and Friedl et al. (2018) for the study period of this analysis. The observed ice thickness changes by this study are in accordance with the remaining accelerated ice discharge of these glaciers, which indicates imbalance conditions. The most pronounced accelerated ice flows as compared to the pre-

270   collapse conditions were reported for Boydell, Sjögren, Drygalski, and Hektoria-Green Glacier. These observations fit well with the high ice thickness change rates in the range of -1.25 to -8.84 m/a found at these glaciers within this study and reported by Rott et al. (2018) for the period 2013-2016. Rott et al. (2018) observed a total mass budget for the analysed glacier area (6358.7 km², Figure 6) of -8.668 ±1.005 Gt/a (1.514 ± 0.176 m/a), which is comparable to our result (observed area: 11685.6 km²) of -7.3 ±0.6 Gt/a (-0.69±0.01 m/a). The total mass budget agrees well. However, the average elevation

275   change rates differ considerably, which can be explained by (1) slightly different observation periods, (2) different glacier outlines, (3) and most important, Rott et al. (2018) analysed only the lower, dynamic outlet glacier tongues (6358.7 km², as compared to 12723.4 km² of the total area of all glaciers, based on the outlines used by the authors). Based on this comparison it can be concluded that the glacier tongues dominate the mass losses of the former tributaries due to the disintegration of the Larsen-A and B ice shelves and that the higher elevated plateau regions show now considerable

280   changes, which is in accordance with Scambos et al. (2014) and our assumption for the coregistration process of the raw TDX DEMs. Moreover, the elevation change patterns on Hektoria-Green Glacier revealed in this analysis support the assumption that wide parts of the lower glacier sections are floating. The distinct change from high surface lowering rates to much smaller rates towards the calving front, indicates that the surface lowering signal by the thinning of the ice is widely compensated by the buoyancy of the ice. A similar, but less pronounced, pattern is also visible at Dinsmoor-Bombardier-

285   Edgewoth (DBE) glacier system and was already discovered by Seehaus et al. (2015). The proposed grounding line position based on our elevation change analysis is also comparable to the one suggested by Rott et al. (2020) for 2016, based on mapping a break in slope for Hektoria-Green Glacier (see Figure 7). At Crane Glacier Rott et al. (2020) suggested as well as grounding line position for 2016. However, our elevation change pattern does not allow a reasonable mapping of such a feature (note: the observed pronounced elevation increase towards the calving front is caused by frontal re-advance). At

290   Wordie Bay (see Figure 7), episodic glacier retreat and acceleration of Fleming Glacier were reported by Friedl et al. (2018), indicating its imbalance. Their suggested grounding line position for 2014 fits partly to the elevation change pattern observed at the lower glacier sections in this study (see Figure 7), similar to Hektoria-Green Glacier.

Scambos et al. (2014) carried out the spatially most extended (<66°S) geodetic analysis on the AP of glacier elevation and mass changes primarily for the period 2003-2008. Due to the difference in the observation periods and the inclusion of the

295 surrounding islands in the regional analysis, a direct comparison of their finding with ours is difficult, in particular, due to dynamic changes of the former ice shelf tributaries along the east coast. However, the general spatial pattern is quite similar. They reported a total mass loss rate of -24.9 Gt/a, -4.7 Gt/a, -2.3 Gt/a, and -18.0 Gt/a for the nAP <66°S, nAP West, nAP North, nAP East (excluding the islands: -20.4 Gt/a, -3.9 Gt/a, -1.8 Gt/a, -14.8 Gt/a; see Scambos et al. (2014) and Figure 6 for region definitions), respectively. Whereas, we observed -11.0±1.2 Gt/a, -3.0±0.7 Gt/a, -0.1±0.0 Gt/a, and -7.8±0.6 Gt/a,

300 respectively. Both analyses obtained similar moderate mass losses for the western sections. For the relatively small nAP North section the difference might be caused by the very limited coverage of the area by DEM data in the study by Scambos et al. (2014). Elevated mass losses are found for the east coast by both analyses, which can be attributed to the imbalance of the former ice shelf tributaries in this section. Reduced mass losses are revealed for the more recent observation period by this study, which is in accordance with other analyses (e.g. Rott et al., 2018; Seehaus et al., 2018).

305 On drainage basin scales a comparison with altimetry, gravimetric, and input-output method-based estimates is feasible. Our revealed results for the different drainage basin definitions are summarized in Table 1. The gravimetric assessment of the mass budget of Antarctica by Groh and Horwath (2021) (https://data1.geo.tu-dresden.de/ais_gmb/) suggests a mass balance for the AIS28 basin definition (corresponding to the 25g and 26g basins) of -5.2 ± 48 Gt/a for the period 2013-06-16 to 2017-06-10, whereas we observed -24.1 ± 2.8 Gt/a. Even though both estimates agree within the error budget, there is a

310 considerable difference in the nominal value. The huge uncertainty of the gravimetric-based estimate clearly indicates the limitations of this approach for the study region. Moreover, the coarse spatial resolution does not allow to resolve detailed spatial patterns or even the analysis of the mass budget on glacier scales. The comparison with altimeter measurements is difficult since most analysis report results only on ice sheet basins scales and for much larger observation periods (e.g. Schröder et al., 2019; Shepherd et al., 2019). However, a meaningful comparison with Smith et al. (2020) is possible. The

315 authors reported a mass budget of -10±2 Gt/a and -16 ± 3 Gt/a for the 25g and 26g basin definitions for the period 2003-2019, respectively. For basin 25g the estimates agree well within the uncertainties with our findings. For basin 26g, they revealed higher mass loss rates. Their analysis starts in 2003, shortly after the disintegration of Larsen-B Ice Self and only a few years after the break-up of Larsen-A and Prince-Gustav-Channel ice shelves. Consequently, the dynamic ice mass loss of the former ice shelf tributaries located in basin 26g and the subsequent adjustments explain the difference to our estimate.

320 Even though the uncertainties are much lower and the spatial resolution is higher than the altimeter based estimates (e.g. 10 km for Schröder et al. (2019), 5 km for Shepherd et al. (2019)) compared to the gravimetric results, the revealed elevation change maps show a blurry pattern hampering more spatially detailed analyses.

Rignot et al. (2019) provides mass balance estimates based on the input-output method on ice sheet basin scales, but also for a few individual glaciers. Thus a comparison on glacier scales is possible, where the individual glaciers could be clearly

325 identified in the inventory used by them and by this study. Based on the supplementary information provided by Rignot et al. (2019), the mass budget was calculated by subtracting the average ice discharge in the years 2013-2017 from the reported

reference SMB. A summary of the comparison with our results, mainly covering glaciers in the Larsen-B embayment, is provided in Table 2. The considerable difference between our estimates of the total mass balance and the results by Rignot et al. (2019) can be partly attributed to differences in the glacier basin definitions. To compensate for the partially strong differences in the glacier basin areas, the specific mass balances were computed. However, for the specific mass balances there are considerable deviations between both estimates as well, even though our estimates agree well with the other geodetic estimates (see above). The limitations in reliable ice thickness estimates towards the grounding lines on the AP (see e.g. Seehaus et al., 2015) and the applied assumptions to overcome these limitations by Rignot et al. (2019) are supposed to strongly bias the mass balance estimations. In particular the assumed balanced conditions for some of the glaciers (Mapple, Pequod, Punchbowl, Starbuck, and Stubb Glacier) by the authors needs to be considered with care. For the SCAR-Inlet tributaries, namely Starbuck and Stubb, and for Pequod Glacier it might be a suitable assumption, however for Mapple and Puchbowl Glacier, this assumption should be revised, considering the specific mass balance estimates (see Table 2). On ice sheet basin scales, a mass budget of -30±28 Gt/a for the I-Ipp basin is revealed by the input-output method, which overlaps with our estimate within the considerable error margins. It can be assumed, that the result is most likely biased by the assumptions made to compensate for the missing good-quality ice thickness information in the study area.

5 Conclusions

By using repeated coverages of the northern AP by bi-static SAR data from austral winters in 2013 and 2017, it was possible to obtain a nearly full coverage (96.4%) of ice surface elevation change measurements throughout the study area. The revealed spatial pattern of glacier changes and the overall mass budget of -24.1±2.8 Gt/a agree well with other analyses. The detailed comparison of the revealed glacier changes at the Larsen-A and B, and Wordie embayments with other published data, based on elevation change measurements, highlights the suitability of the applied approach and the quality of the obtained results. However, the comparison with estimates based on the input-output method revealed strong deviations, in particular on glacier scales. These findings stress the need for improved ice thickness data towards the grounding line along the AP, which is the dominating error source in ice discharge estimates on the AP.

By including information on climatic mass balance, it could be identified that the observed mass changes can be, at least partly, attributed to climatic mass balance variations, for wide parts of the southern section of the study area. However, most of the revealed mass losses are caused by ice dynamic changes. In particular, the still ongoing increased ice discharge at the former ice shelf tributaries at the Prince-Gustav-Channel, Larsen-A&B, and Wordie ice shelves are the hot-spots of mass loss, and 67% of the total mass loss throughout the study area can be attributed to these regions.

The previously reported correlation between increased frontal recession and mid-ocean warming along the south-western coast of the study area could not be repeated by the surface elevation or mass change pattern observed in this analysis, excluding Wordie Bay. Probably, the ice flow of the well-confined glacier tongues in the fjord-like valleys did not get destabilized by the frontal retreat. In order to backup this assumption and to further analyse the obtained glacier changes and

its driving factors, a detailed analysis of the evolution of the ice dynamics throughout the study area would be desirable, which is, however, beyond the scope of this analysis.

This study provides the first geodetic assessment of glacier mass balances base on DEM differentiating throughout the northern AP at unprecedented spatially detailed scales and with high precision. The findings allow ice elevation change and mass budget estimates on ice sheet basins as well as individual glacier scales, which will be beneficial for glaciological modelling, like enhanced ice thickness reconstructions, and continental and global estimates of ice mass changes and sea level rise computations.

Author Contributions: TS initiated, designed and led the study, processed and analysed the data and wrote the manuscript. TS, PM and CS developed jointly the analysis routines for elevation change and mass balance computations. TD contributed the MAR data and CMB analysis. All authors revised the manuscript.

Competing interests: The authors declare no conflict of interest. The founding sponsors had no role in the design of the study; in the collection, analysis, or interpretation of data; in the writing of the manuscript, and in the decision to publish the results.

Acknowledgements: This work was financially supported by the ESA Living Planet Fellowship MIT-AP granted to TS and the priority programme "Regional Sea Level Change and Society" by the grant DFG BR2105/14-2. The authors would like to thank the German Aerospace Center for providing TanDEM-X data free of charge under AO XTI_GLAC0264. A. Silva kindly provided the glacier inventory of the AP from Silva et al. (2020). P. Friedl kindly provided the groundling line data from Friedl et al. (2018). The TanDEM-X DEM of the AP used as reference was kindly provided by D. Floricioiu. ERA-5 reanalysis data (Hersbach et al., 2020) are provided by the European Centre for Medium-Range Weather Forecasts, from their website at https:// www.ecmwf.int/en/forecasts/datasets/reanalysis-datasets/era5 (last ac- cess: 24 October 2022). Computer resources were provided by Consortium des Équipements de Calcul Intensif (CÉCI), funded by the Fonds de la Recherche Scientifique de Belgique (F.R.S. – FNRS) under grant no. 2.5020.11 and the Tier-1 supercomputer (Nic5) of the Fédération Wallonie Bruxelles infrastructure funded by the Walloon Region under grant agreement no. 1117545. Special thanks to Christoph Kittel for the help on the MAR data processing and evaluation.

Code availability: The code for the MAR data used in this study is tagged as v3.12 on https://gitlab.com/Mar-Group/MARv3 (MAR model, 2022). Instructions to download the MAR code are provided on https://www.mar.cnrs.fr (MAR Team, 2022).

Data availability: Elevation change fields are available via the World Data Center PANGAEA operated by AWI Bremerhaven (after publication of the manuscript). The MAR outputs used in this study are available upon request by email (tdethinne@uliege.be).

References

Abdel Jaber, W., Rott, H., Floricioiu, D., Wuite, J., Miranda, N., 2019. Heterogeneous spatial and temporal pattern of surface elevation change and mass balance of the Patagonian ice fields between 2000 and 2016. The Cryosphere 13, 2511–2535. https://doi.org/10.5194/tc-13-2511-2019

Abdullahi, S., Wessel, B., Leichtle, T., Huber, M., Wohlfart, C., Roth, A., 2018. Investigation of Tandem-x Penetration Depth Over the Greenland Ice Sheet, in: IGARSS 2018 - 2018 IEEE International Geoscience and Remote Sensing Symposium. Presented at the IGARSS 2018 - 2018 IEEE International Geoscience and Remote Sensing Symposium, pp. 1336–1339. https://doi.org/10.1109/IGARSS.2018.8518930

Amory, C., Kittel, C., Le Toumelin, L., Agosta, C., Delhasse, A., Favier, V., Fettweis, X., 2021. Performance of MAR (v3.11) in simulating the drifting-snow climate and surface mass balance of Adélie Land, East Antarctica. Geosci. Model Dev. 14, 3487–3510. https://doi.org/10.5194/gmd-14-3487-2021

Braun, M.H., Malz, P., Sommer, C., Farías-Barahona, D., Sauter, T., Casassa, G., Soruco, A., Skvarca, P., Seehaus, T.C., 2019. Constraining glacier elevation and mass changes in South America. Nature Climate Change 1. https://doi.org/10.1038/s41558-018-0375-7

Brun, F., Berthier, E., Wagnon, P., Kääb, A., Treichler, D., 2017. A spatially resolved estimate of High Mountain Asia glacier mass balances from 2000 to 2016. Nature Geoscience 10, 668. https://doi.org/10.1038/ngeo2999

Carrasco, J.F., Bozkurt, D., Cordero, R.R., 2021. A review of the observed air temperature in the Antarctic Peninsula. Did the warming trend come back after the early 21st hiatus? Polar Science, SuperDARN / Studies of Geospace Dynamics - Today and Future 28, 100653. https://doi.org/10.1016/j.polar.2021.100653

Cook, A.J., Holland, P.R., Meredith, M.P., Murray, T., Luckman, A., Vaughan, D.G., 2016. Ocean forcing of glacier retreat in the western Antarctic Peninsula. Science 353, 283–286. https://doi.org/10.1126/science.aae0017

Cook, A.J., Vaughan, D.G., 2010. Overview of areal changes of the ice shelves on the Antarctic Peninsula over the past 50 years. The Cryosphere 4, 77–98. https://doi.org/10.5194/tc-4-77-2010

De Ridder, K., Gallée, H., 1998. Land Surface–Induced Regional Climate Change in Southern Israel. Journal of Applied Meteorology (1988-2005) 37, 1470–1485.

Delhasse, A., Kittel, C., Amory, C., Hofer, S., van As, D., S. Fausto, R., Fettweis, X., 2020. Brief communication: Evaluation of the near-surface climate in ERA5 over the Greenland Ice Sheet. The Cryosphere 14, 957–965. https://doi.org/10.5194/tc-14-957-2020

Dethinne, T., Glaude, Q., Picard, G., Kittel, C., Orban, A., Fettweis, X., 2022. Assimilation sensitivity of satellite-derived surface melt into the Regional Climate Model MAR: case study over the Antarctic Peninsula. EGUsphere 1–31. https://doi.org/10.5194/egusphere-2022-1371

Dong, Y., Zhao, J., Floricioiu, D., Krieger, L., Fritz, T., Eineder, M., 2021. High-resolution topography of the Antarctic Peninsula combining the TanDEM-X DEM and Reference Elevation Model of Antarctica (REMA) mosaic. The Cryosphere 15, 4421–4443. https://doi.org/10.5194/tc-15-4421-2021

Dussaillant, I., Berthier, E., Brun, F., Masiokas, M., Hugonnet, R., Favier, V., Rabatel, A., Pitte, P., Ruiz, L., 2019. Two decades of glacier mass loss along the Andes. Nat. Geosci. 1–7. https://doi.org/10.1038/s41561-019-0432-5

Ferrigno, J.G., Cook, A.J., Foley, K.M., Williams, R.S., Swithinbank, C., Fox, A.J., Thomson, J.W., Sievers, J., 2006. Coastal-change and glaciological map of the Trinity Peninsula area and South Shetland Islands, Antarctica, 1843-2001.

Fettweis, X., Hofer, S., Séférian, R., Amory, C., Delhasse, A., Doutreloup, S., Kittel, C., Lang, C., Van Bever, J., Veillon, F., Irvine, P., 2021. Brief communication: Reduction in the future Greenland ice sheet surface melt with the help of solar geoengineering. The Cryosphere 15, 3013–3019. https://doi.org/10.5194/tc-15-3013-2021

Friedl, P., Seehaus, T.C., Wendt, A., Braun, M.H., Höppner, K., 2018. Recent dynamic changes on Fleming Glacier after the disintegration of Wordie Ice Shelf, Antarctic Peninsula. The Cryosphere 12, 1347–1365. https://doi.org/10.5194/tc-12-1347-2018

Gallée, H., Schayes, G., 1994. Development of a Three-Dimensional Meso-γ Primitive Equation Model: Katabatic Winds Simulation in the Area of Terra Nova Bay, Antarctica. Monthly Weather Review 122, 671–685. https://doi.org/10.1175/1520-0493(1994)122<0671:DOATDM>2.0.CO;2

Gilbert, E., Kittel, C., 2021. Surface Melt and Runoff on Antarctic Ice Shelves at 1.5°C, 2°C, and 4°C of Future Warming. Geophysical Research Letters 48. https://doi.org/10.1029/2020GL091733

Groh, A., Horwath, M., 2021. Antarctic Ice Mass Change Products from GRACE/GRACE-FO Using Tailored Sensitivity Kernels. Remote Sensing 13, 1736. https://doi.org/10.3390/rs13091736

Hersbach, H., Bell, B., Berrisford, P., Hirahara, S., Horányi, A., Muñoz-Sabater, J., Nicolas, J., Peubey, C., Radu, R., Schepers, D., Simmons, A., Soci, C., Abdalla, S., Abellan, X., Balsamo, G., Bechtold, P., Biavati, G., Bidlot, J., Bonavita, M., De Chiara, G., Dahlgren, P., Dee, D., Diamantakis, M., Dragani, R., Flemming, J., Forbes, R., Fuentes, M., Geer, A., Haimberger, L., Healy, S., Hogan, R.J., Hólm, E., Janisková, M., Keeley, S., Laloyaux, P., Lopez, P., Lupu, C., Radnoti, G., de Rosnay, P., Rozum, I., Vamborg, F., Villaume, S., Thépaut, J.-N., 2020. The ERA5 global reanalysis. Quarterly Journal of the Royal Meteorological Society 146, 1999–2049. https://doi.org/10.1002/qj.3803

Hogg, A.E., Gudmundsson, G.H., 2017. Impacts of the Larsen-C Ice Shelf calving event. Nature Climate Change 7, 540–542. https://doi.org/10.1038/nclimate3359

Hogg, A.E., Shepherd, A., Cornford, S.L., Briggs, K.H., Gourmelen, N., Graham, J.A., Joughin, I., Mouginot, J., Nagler, T., Payne, A.J., Rignot, E., Wuite, J., 2017. Increased ice flow in Western Palmer Land linked to ocean melting. Geophys. Res. Lett. 2016GL072110. https://doi.org/10.1002/2016GL072110

Holland, P.R., Brisbourne, A., Corr, H.F.J., McGrath, D., Purdon, K., Paden, J., Fricker, H.A., Paolo, F.S., Fleming, A.H., 2015. Oceanic and atmospheric forcing of Larsen C Ice-Shelf thinning. The Cryosphere 9, 1005–1024. https://doi.org/10.5194/tc-9-1005-2015

Holland, P.R., Jenkins, A., Holland, D.M., 2010. Ice and ocean processes in the Bellingshausen Sea, Antarctica. J. Geophys. Res. 115, C05020. https://doi.org/10.1029/2008JC005219

Horwath, M., Dietrich, R., 2009. Signal and error in mass change inferences from GRACE: the case of Antarctica. Geophys J Int 177, 849–864. https://doi.org/10.1111/j.1365-246X.2009.04139.x

Howat, I.M., Porter, C., Smith, B.E., Noh, M.-J., Morin, P., 2019. The Reference Elevation Model of Antarctica. The Cryosphere 13, 665–674. https://doi.org/10.5194/tc-13-665-2019

Hugonnet, R., McNabb, R., Berthier, E., Menounos, B., Nuth, C., Girod, L., Farinotti, D., Huss, M., Dussaillant, I., Brun, F., Kääb, A., 2021. Accelerated global glacier mass loss in the early twenty-first century. Nature 592, 726–731. https://doi.org/10.1038/s41586-021-03436-z

Huss, M., 2013. Density assumptions for converting geodetic glacier volume change to mass change. The Cryosphere 7, 877–887. https://doi.org/10.5194/tc-7-877-2013

IMBIE Team, 2018. Mass balance of the Antarctic Ice Sheet from 1992 to 2017. Nature 558, 219. https://doi.org/10.1038/s41586-018-0179-y

Kääb, A., Berthier, E., Nuth, C., Gardelle, J., Arnaud, Y., 2012. Contrasting patterns of early twenty-first-century glacier mass change in the Himalayas. Nature 488, 495–498. https://doi.org/10.1038/nature11324

Kittel, C., Amory, C., Agosta, C., Jourdain, N.C., Hofer, S., Delhasse, A., Doutreloup, S., Huot, P.-V., Lang, C., Fichefet, T., Fettweis, X., 2021. Diverging future surface mass balance between the Antarctic ice shelves and grounded ice sheet. The Cryosphere 15, 1215–1236. https://doi.org/10.5194/tc-15-1215-2021

Lambin, C., Fettweis, X., Kittel, C., Fonder, M., Ernst, D., 2022. Assessment of future wind speed and wind power changes over South Greenland using the MODÈLE ATMOSPHÉRIQUE RÉGIONAL regional climate model. Intl Journal of Climatology joc.7795. https://doi.org/10.1002/joc.7795

Malz, P., Meier, W., Casassa, G., Jaña, R., Skvarca, P., Braun, M.H., 2018. Elevation and Mass Changes of the Southern Patagonia Icefield Derived from TanDEM-X and SRTM Data. Remote Sensing 10, 188. https://doi.org/10.3390/rs10020188

Morcrette, J.-J., 2002. Assessment of the ECMWF Model Cloudiness and Surface Radiation Fields at the ARM SGP Site. Monthly Weather Review 130, 257–277.

Mouginot, J., Rignot, E., Scheuchl, B., Millan, R., 2017. Comprehensive Annual Ice Sheet Velocity Mapping Using Landsat-8, Sentinel-1, and RADARSAT-2 Data. Remote Sensing 9, 364. https://doi.org/10.3390/rs9040364

Nuth, C., Kääb, A., 2011. Co-registration and bias corrections of satellite elevation data sets for quantifying glacier thickness change. The Cryosphere 5, 271–290. https://doi.org/10.5194/tc-5-271-2011

Oliva, M., Navarro, F., Hrbáček, F., Hernández, A., Nývlt, D., Pereira, P., Ruiz-Fernández, J., Trigo, R., 2017. Recent regional climate cooling on the Antarctic Peninsula and associated impacts on the cryosphere. Science of The Total Environment 580, 210–223. https://doi.org/10.1016/j.scitotenv.2016.12.030

Rignot, E., Mouginot, J., Scheuchl, B., 2011. Ice Flow of the Antarctic Ice Sheet. Science 333, 1427–1430. https://doi.org/10.1126/science.1208336

490   Rignot, E., Mouginot, J., Scheuchl, B., Broeke, M. van den, Wessem, M.J. van, Morlighem, M., 2019. Four decades of Antarctic Ice Sheet mass balance from 1979–2017. PNAS 201812883. https://doi.org/10.1073/pnas.1812883116

Rolstad, C., Haug, T., Denby, B., 2009. Spatially integrated geodetic glacier mass balance and its uncertainty based on geostatistical analysis: application to the western Svartisen ice cap, Norway. Journal of Glaciology 55, 666–680. https://doi.org/10.3189/002214309789470950

495   Rott, H., Abdel Jaber, W., Wuite, J., Scheiblauer, S., Floricioiu, D., van Wessem, J.M., Nagler, T., Miranda, N., van den Broeke, M.R., 2018. Changing pattern of ice flow and mass balance for glaciers discharging into the Larsen A and B embayments, Antarctic Peninsula, 2011 to 2016. The Cryosphere 12, 1273–1291. https://doi.org/10.5194/tc-12-1273-2018

Rott, H., Floricioiu, D., Wuite, J., Scheiblauer, S., Nagler, T., Kern, M., 2014. Mass changes of outlet glaciers along the
500   Nordensjköld Coast, northern Antarctic Peninsula, based on TanDEM-X satellite measurements. Geophys. Res. Lett. 2014GL061613. https://doi.org/10.1002/2014GL061613

Rott, H., Müller, F., Nagler, T., Floricioiu, D., 2011. The imbalance of glaciers after disintegration of Larsen-B ice shelf, Antarctic Peninsula. The Cryosphere 5, 125–134. https://doi.org/10.5194/tc-5-125-2011

Rott, H., Scheiblauer, S., Wuite, J., Krieger, L., Floricioiu, D., Rizzoli, P., Libert, L., Nagler, T., 2021. Penetration of
505   interferometric radar signals in Antarctic snow. The Cryosphere Discussions 1–27. https://doi.org/10.5194/tc-2020-380

Rott, H., Wuite, J., De Rydt, J., Gudmundsson, G.H., Floricioiu, D., Rack, W., 2020. Impact of marine processes on flow dynamics of northern Antarctic Peninsula outlet glaciers. Nature Communications 11, 2969. https://doi.org/10.1038/s41467-020-16658-y

510   Scambos, T., Hulbe, C., Fahnestock, M., 2003. Climate-Induced Ice Shelf Disintegration in the Antarctic Peninsula, in: Domack, E., Levente, A., Burnet, A., Bindschadler, R., Convey, P., Kirby, tthew (Eds.), Antarctic Peninsula Climate Variability: Historical and Paleoenvironmental Perspectives. American Geophysical Union, pp. 79–92.

Scambos, T.A., 2004. Glacier acceleration and thinning after ice shelf collapse in the Larsen B embayment, Antarctica. Geophysical Research Letters 31. https://doi.org/10.1029/2004GL020670

515   Scambos, T.A., Berthier, E., Haran, T., Shuman, C.A., Cook, A.J., Ligtenberg, S.R.M., Bohlander, J., 2014. Detailed ice loss pattern in the northern Antarctic Peninsula: widespread decline driven by ice front retreats. The Cryosphere 8, 2135–2145. https://doi.org/10.5194/tc-8-2135-2014

Schröder, L., Horwath, M., Dietrich, R., Helm, V., Broeke, M.R. van den, Ligtenberg, S.R.M., 2019. Four decades of Antarctic surface elevation changes from multi-mission satellite altimetry. The Cryosphere 13, 427–449.
520   https://doi.org/10.5194/tc-13-427-2019

Seehaus, T., Cook, A.J., Silva, A.B., Braun, M., 2018. Changes in glacier dynamics in the northern Antarctic Peninsula since 1985. The Cryosphere 12, 577–594. https://doi.org/10.5194/tc-12-577-2018

Seehaus, T., Malz, P., Sommer, C., Lippl, S., Cochachin, A., Braun, M., 2019. Changes of the tropical glaciers throughout Peru between 2000 and 2016 – mass balance and area fluctuations. The Cryosphere 13, 2537–2556. https://doi.org/10.5194/tc-13-2537-2019

Seehaus, T., Malz, P., Sommer, C., Soruco, A., Rabatel, A., Braun, M., 2020a. Mass balance and area changes of glaciers in the Cordillera Real and Tres Cruces, Bolivia, between 2000 and 2016. Journal of Glaciology 66, 124–136. https://doi.org/10.1017/jog.2019.94

Seehaus, T., Marinsek, S., Helm, V., Skvarca, P., Braun, M., 2015. Changes in ice dynamics, elevation and mass discharge of Dinsmoor–Bombardier–Edgeworth glacier system, Antarctic Peninsula. Earth and Planetary Science Letters 427, 125–135.

Seehaus, T., Morgenshtern, V.I., Hübner, F., Bänsch, E., Braun, M.H., 2020b. Novel Techniques for Void Filling in Glacier Elevation Change Data Sets. Remote Sensing 12, 3917. https://doi.org/10.3390/rs12233917

Seehaus, T.C., Marinsek, S., Skvarca, P., van Wessem, J.M., Reijmer, C.H., Seco, J.L., Braun, M.H., 2016. Dynamic Response of Sjögren Inlet Glaciers, Antarctic Peninsula, to Ice Shelf Breakup Derived from Multi-Mission Remote Sensing Time Series. Frontiers in Earth Science 4. https://doi.org/10.3389/feart.2016.00066

Shepherd, A., Gilbert, L., Muir, A.S., Konrad, H., McMillan, M., Slater, T., Briggs, K.H., Sundal, A.V., Hogg, A.E., Engdahl, M.E., 2019. Trends in Antarctic Ice Sheet Elevation and Mass. Geophysical Research Letters 46, 8174–8183. https://doi.org/10.1029/2019GL082182

Silva, A.B., Arigony-Neto, J., Braun, M.H., Espinoza, J.M.A., Costi, J., Janã, R., 2020. Spatial and temporal analysis of changes in the glaciers of the Antarctic Peninsula. Global and Planetary Change 184, 103079. https://doi.org/10.1016/j.gloplacha.2019.103079

Smith, B., Fricker, H.A., Gardner, A.S., Medley, B., Nilsson, J., Paolo, F.S., Holschuh, N., Adusumilli, S., Brunt, K., Csatho, B., Harbeck, K., Markus, T., Neumann, T., Siegfried, M.R., Zwally, H.J., 2020. Pervasive ice sheet mass loss reflects competing ocean and atmosphere processes. Science. https://doi.org/10.1126/science.aaz5845

Sommer, C., Seehaus, T., Glazovsky, A., Braun, M.H., 2022. Brief communication: Increased glacier mass loss in the Russian High Arctic (2010–2017). The Cryosphere 16, 35–42. https://doi.org/10.5194/tc-16-35-2022

Toutin, T., 2002. Three-dimensional topographic mapping with ASTER stereo data in rugged topography. IEEE Transactions on Geoscience and Remote Sensing 40, 2241–2247. https://doi.org/10.1109/TGRS.2002.802878

Turner, J., Lu, H., White, I., King, J.C., Phillips, T., Hosking, J.S., Bracegirdle, T.J., Marshall, G.J., Mulvaney, R., Deb, P., 2016. Absence of 21st century warming on Antarctic Peninsula consistent with natural variability. Nature 535, 411–415. https://doi.org/10.1038/nature18645

Vaughan, D.G., Marshall, G.J., Connolley, W.M., Parkinson, C., Mulvaney, R., Hodgson, D.A., King, J.C., Pudsey, C.J., Turner, J., 2003. Recent rapid regional climate warming on the Antarctic Peninsula. Climatic change 60, 243–274.

555   Walker, C.C., Gardner, A.S., 2017. Rapid drawdown of Antarctica's Wordie Ice Shelf glaciers in response to ENSO/Southern Annular Mode-driven warming in the Southern Ocean. Earth and Planetary Science Letters 476, 100–110. https://doi.org/10.1016/j.epsl.2017.08.005

   Wendt, J., Rivera, A., Wendt, A., Bown, F., Zamora, R., Casassa, G., Bravo, C., 2010. Recent ice-surface-elevation changes of Fleming Glacier in response to the removal of the Wordie Ice Shelf, Antarctic Peninsula. Annals of Glaciology
560   51, 97–102.

   Wouters, B., Martin-Español, A., Helm, V., Flament, T., Wessem, J.M. van, Ligtenberg, S.R.M., Broeke, M.R. van den, Bamber, J.L., 2015. Dynamic thinning of glaciers on the Southern Antarctic Peninsula. Science 348, 899–903. https://doi.org/10.1126/science.aaa5727

   Wuite, J., Rott, H., Hetzenecker, M., Floricioiu, D., De Rydt, J., Gudmundsson, G.H., Nagler, T., Kern, M., 2015. Evolution
565   of surface velocities and ice discharge of Larsen B outlet glaciers from 1995 to 2013. The Cryosphere 9, 957–969. https://doi.org/10.5194/tc-9-957-2015

   Zwally, H.J., Giovinetto, M., Beckley, M.A., Saba, J.L., 2012. Antarctic and Greenland Drainage Systems.

570
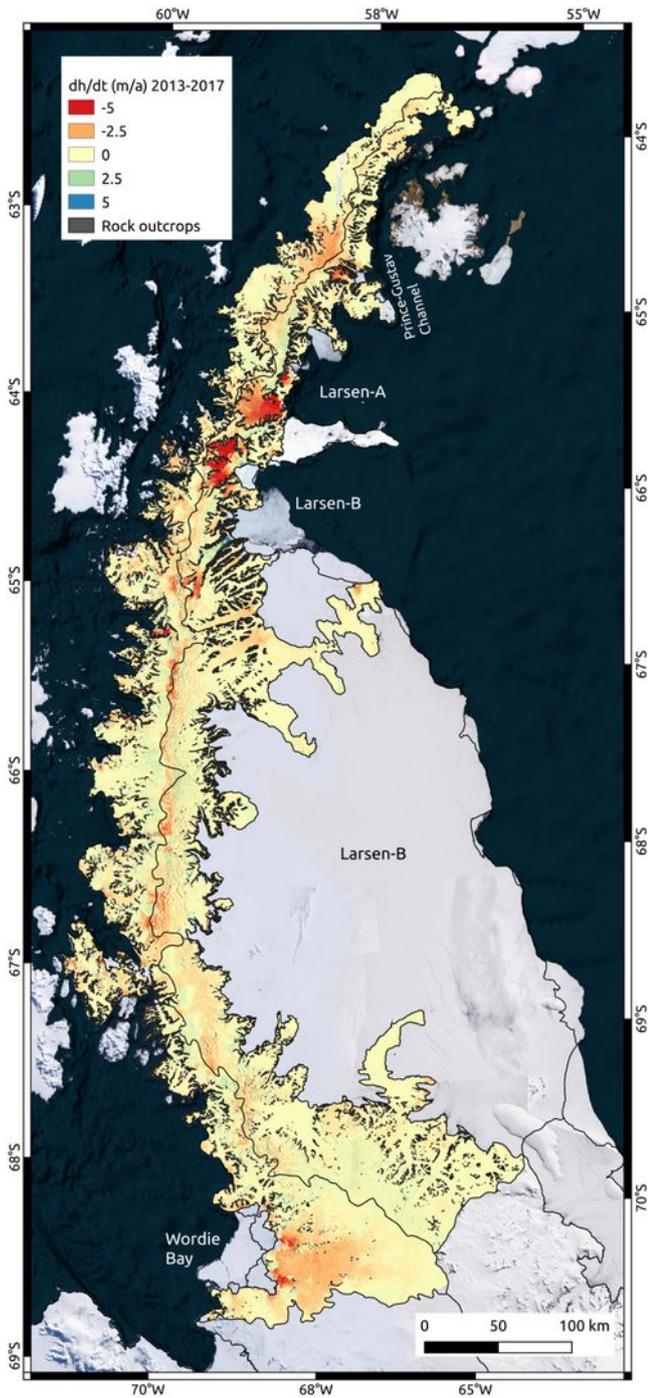
Figure 1. Surface elevation changes between austral-winter of 2013 and 2017 derived from TanDEM-X acquisitions for the 25g and 26g basin according to Zwally et al. (2012). Background: © Bing Satellite map by Microsoft; Black polygons: rock-outcrops according to Silva et al. (2020)
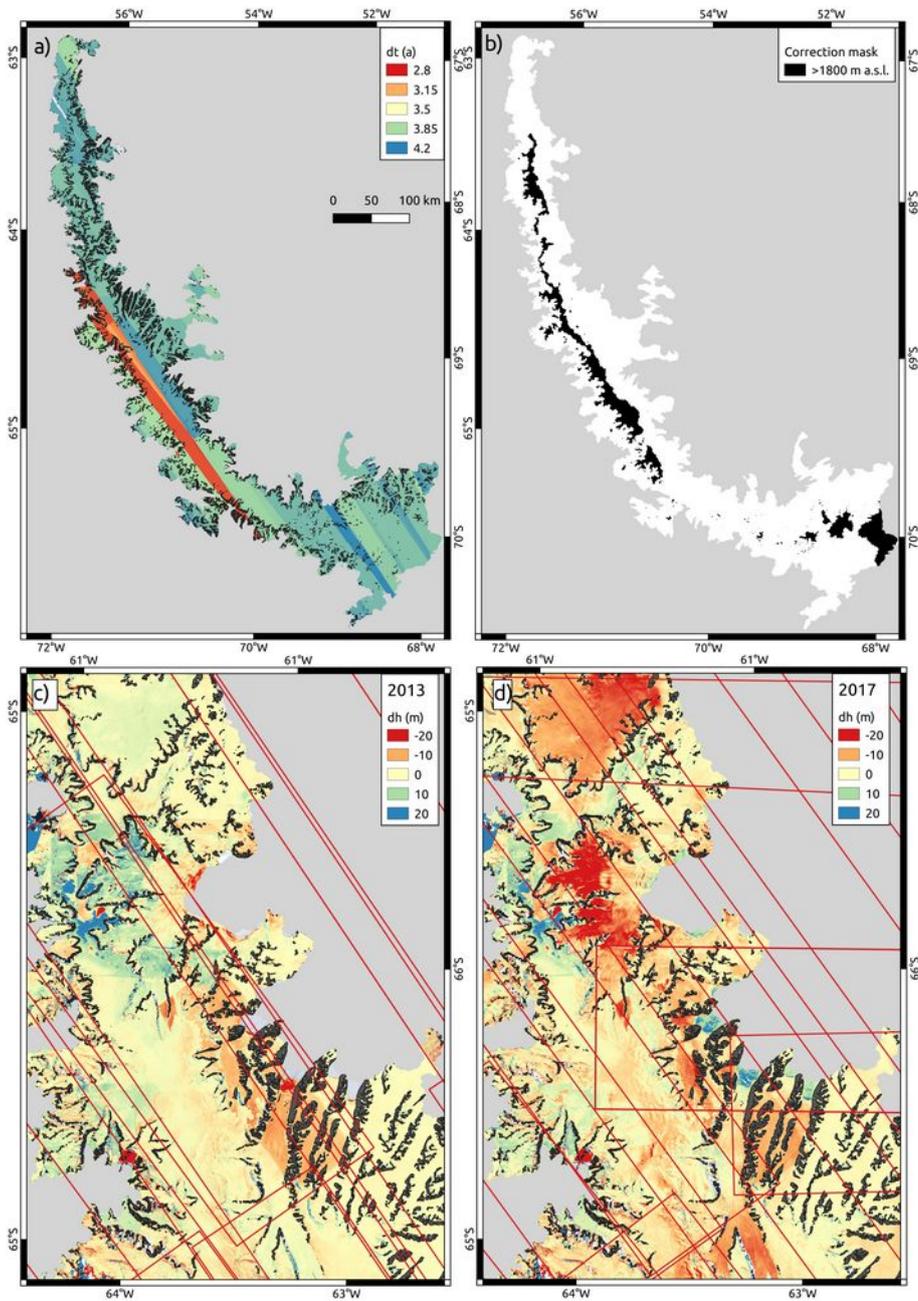
Figure 2. a) Time difference between elevation measurements b) Mask of areas above 1800 m a.s.l. used for radar penetration bias correction. c) Election difference between refDEM and DEMs obtained in this study for 2013 and de) for 2017. Black polygons: rock-outcrops according to Silva et al. (2020)
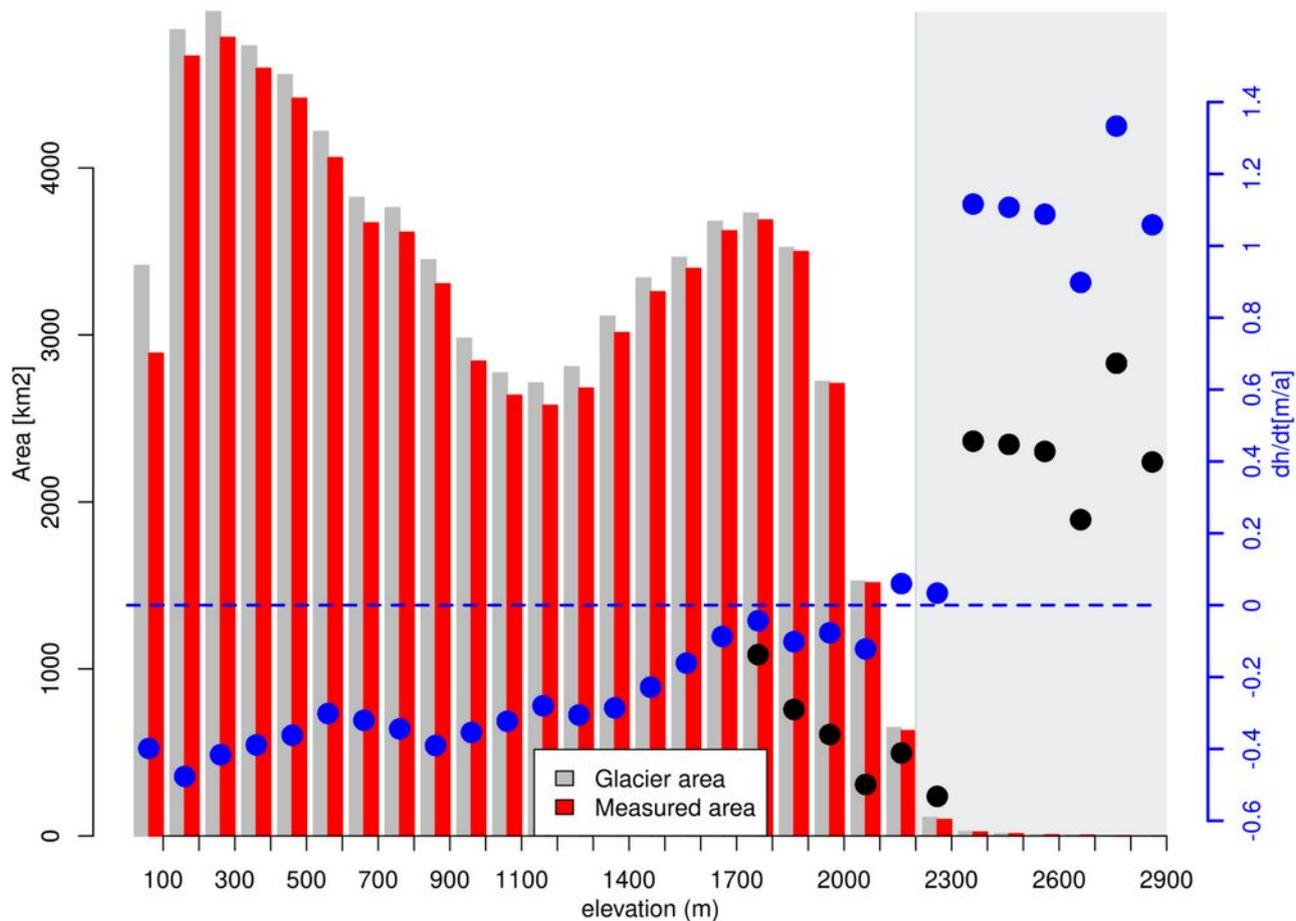
Figure 3. Hypsometric distribution of measured (red bars) and total (grey bars) glacier area of 25g and 26g basins. Blue dots represent the mean Δh/Δt value in each elevation interval, including corrections in areas above 1800 m a.s.l. Black dots indicate the uncorrected Δh/Δt values. Grey area marks~~areas mark~~ the upper 1% quantile of the total glacier area distribution. Note: The scattered Δh/Δt values in areas above 2300 m a.s.l. are located around one peak towards the southern border of the study area, where the steep slope most likely lead to some biases. The affected area corresponds to only 0.06% of the total glacier area, and thus its impact on the total mass budget can be neglected

585
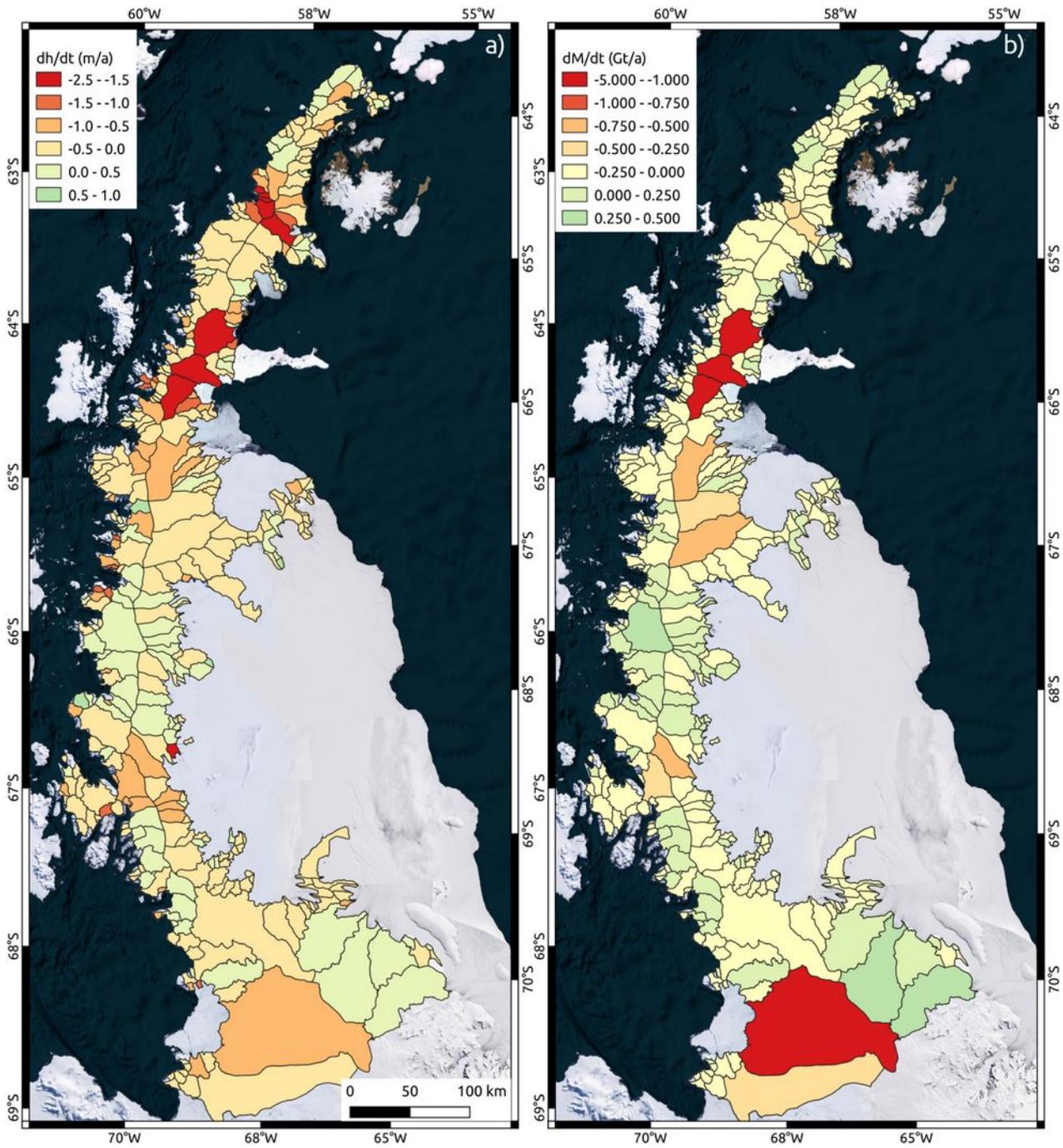
590

Figure 4. a) Average surface elevation changes (dh/dt) and b) total mass changes (dM/dt) for individual glaciers >20km²
Background: © Bing Satellite map by Microsoft
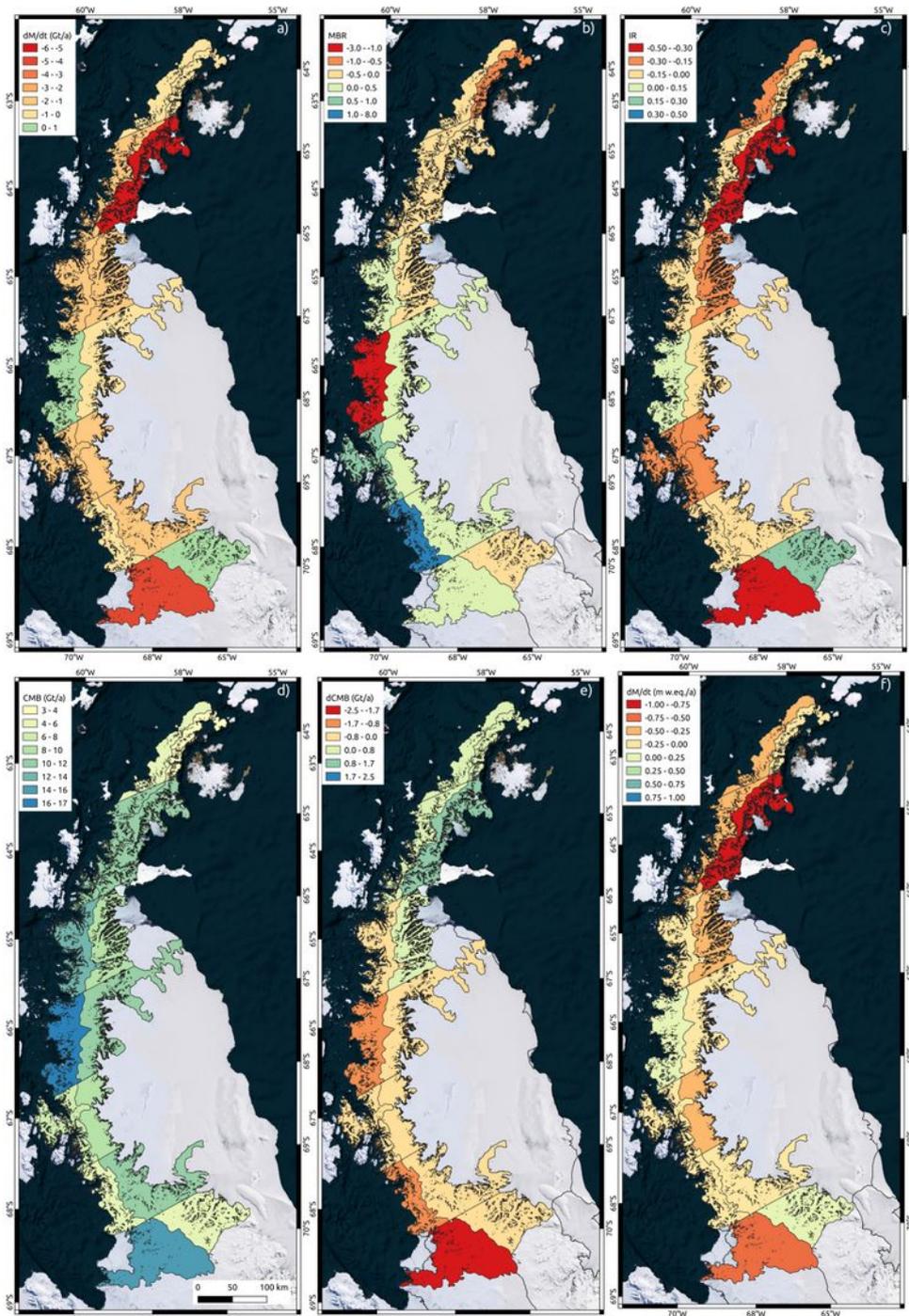
Figure 5. a) Total mass balance, b) mass balance ratio, c) imbalance ration, d) total climatic mass balance, e) total climatic mass balance anomalies, and f) specific mass balance for latitudinal subsets of the 25g and 26g drainage basins. Background: © Bing Satellite map by Microsoft; Black polygons: rock-outcrops according to Silva et al. (2020)
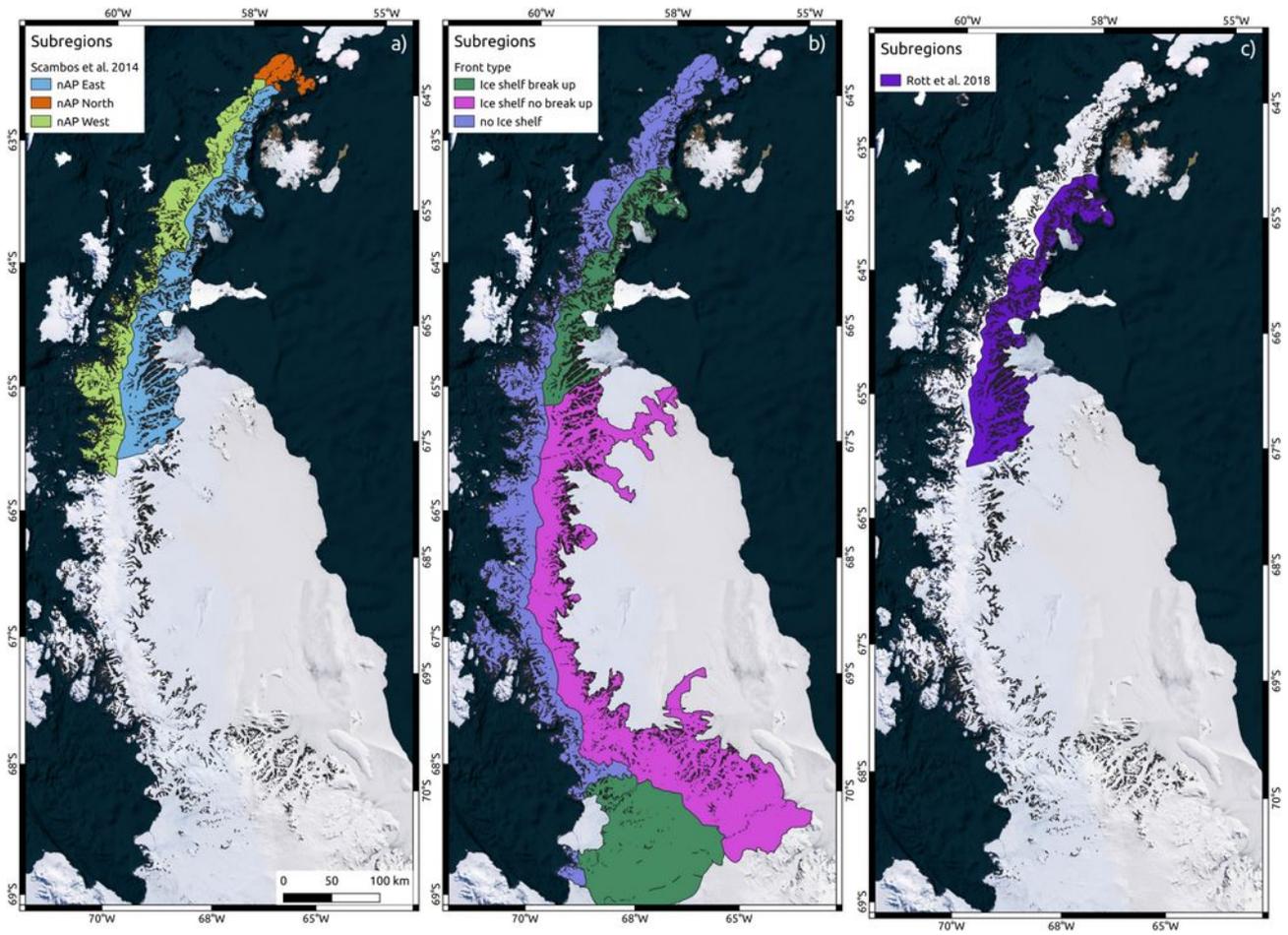
Figure 6. Sub-regions of the total study side based on a) Scambos et al. (2014), b) glacier front type, and c) Rott et al. (2018). Background: © Bing Satellite map by Microsoft; Black polygons: rock-outcrops according to Silva et al. (2020)
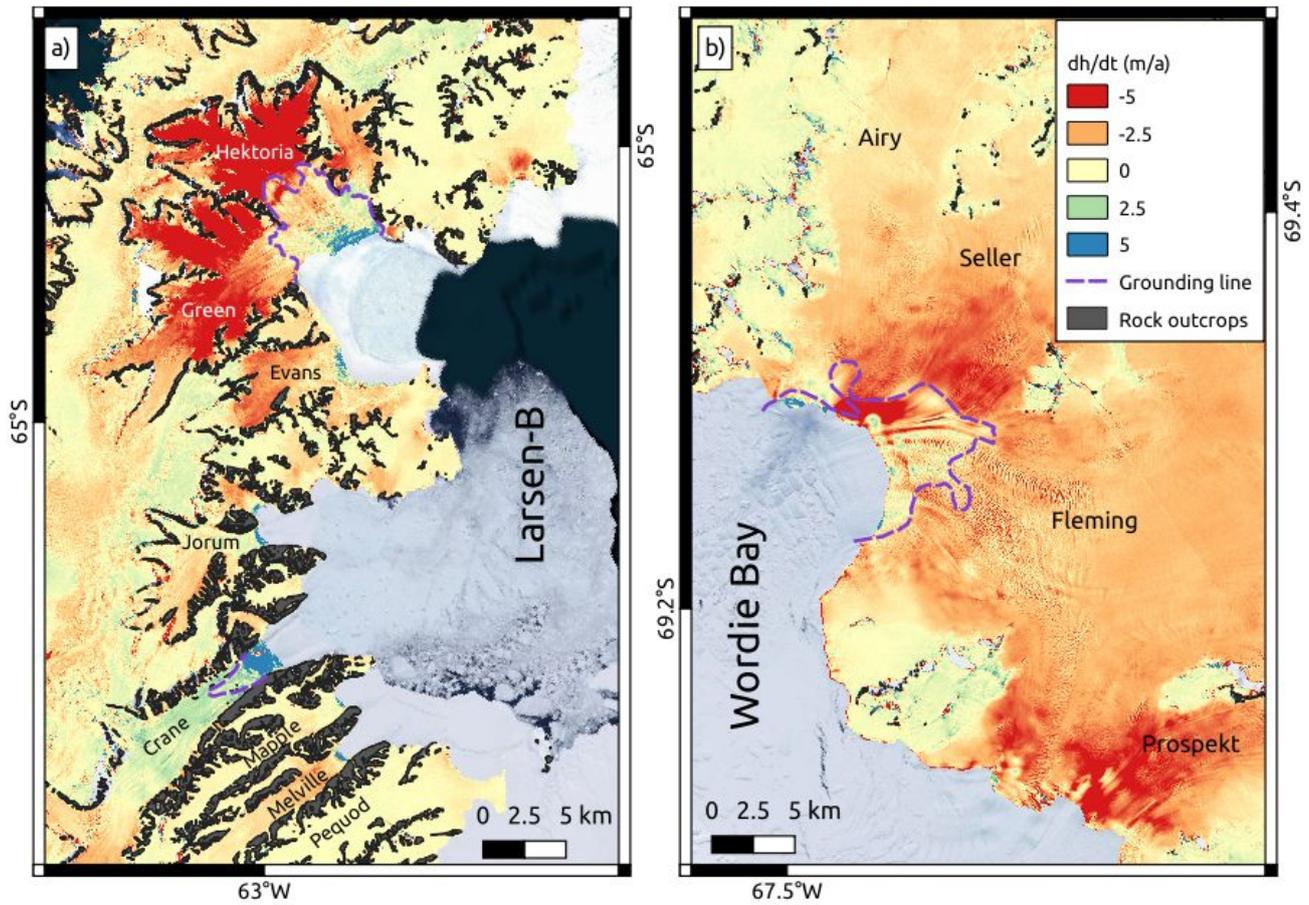
Figure 7. Grounding line positions at Hektoria-Green-Evans and Crane glaciers in 2016 from Rott et al. (2018), and b) Airy-Seller-Fleming Glacier for 2014 from Friedl et al. (2018) overlaid on the derived surface elevation changes between 2013 and 2017. Background: © Bing Satellite map by Microsoft; Black polygons: rock-outcrops according to Silva et al. (2020)

Table 1: Summary of analyzed glacier area (S), glacier area covered by measurements (SM), average surface lowering rate ($\Delta h/\Delta t$) (note: the listed uncertainty of $\Delta h/\Delta t$ represent the slope-weighted average offsets on rock-outcrops including consideration of spatial auto-correlation, but not SAR-signal penetration correction), total mass budget ($\Delta M/\Delta t$), average climatic mass balance (CMB), imbalance ratio (IR), and mass balance ratio (MBR) for different basin and subregion definitions. *Subregion definitions according to Scambos et al. (2014), +Subregion definitions based on glacier front type: No IS: non ice shelf tributaries, IS break: former ice shelf tributaries, IS no break: current ice shelf tributaries; °Subregion definition according to Rott et al. (2018)

Basin/ Subreg.	Lat.	S (km²)	S_m (km²)	$\Delta h/\Delta t$ (m/a)	$\Delta M/\Delta t$ (Gt/a)	CMB (m w.e./a)	CMB (Gt/a)	IR	MBR
25g&26g	total	74888.0	72222.1	-0.283±0.003	-24.1±2.8	1.72	128.0	-0.19	0.19
25g	total	34474.5	32952.6	-0.295±0.007	-12.2±1.7	2.21	71.9	-0.17	0.43
	63	3184.2	3035.2	-0.341±0.023	-1.0±0.1	1.80	5.4	-0.18	-0.34
	64	4273.1	4068.8	-0.354±0.023	-1.4±0.2	2.39	10.1	-0.14	-0.20
	65	4903.3	4545.5	-0.253±0.028	-1.1±0.4	2.74	13.4	-0.08	0.46
	66	5607.8	5404.5	0.079±0.023	0.4±0.4	2.92	16.1	0.02	-3.03
	67	4195.1	3854.6	-0.283±0.018	-1.1±0.1	1.61	7.1	-0.15	0.73
	68	3511.7	3430.0	-0.042±0.017	-0.1±0.1	1.58	5.6	-0.02	7.75
	69	8799.2	8613.9	-0.607±0.010	-4.8±0.6	1.61	14.1	-0.34	0.49
26g	total	40413.5	39269.5	-0.276±0.004	-12.0±1.2	1.34	57.4	-0.21	-0.04
	63	2185.8	2139.0	-0.261±0.008	-0.5±0.0	1.68	3.6	-0.14	-0.92
	64	6030.0	5674.3	-0.950±0.012	-5.2±0.4	1.89	11.5	-0.45	-0.21
	65	5467.8	5308.6	-0.390±0.016	-1.9±0.2	1.41	8.1	-0.24	-0.19
	66	8578.0	8418.7	-0.101±0.009	-0.8±0.3	1.29	11.1	-0.07	0.17
	67	4174.9	3950.5	-0.364±0.018	-1.4±0.1	2.00	8.2	-0.17	0.45
	68	7581.2	7411.0	-0.164±0.009	-1.1±0.1	1.33	10.1	-0.11	0.47
	69	6395.8	6367.3	0.137±0.003	0.8±0.3	0.72	4.6	0.17	-0.20
I-Ipp	total	58985.4	56351.5	-0.277±0.004	-14.7±2.0	1.83	108.3	-0.14	0.13
	63	5371.9	5173.3	-0.309±0.006	-1.5±0.1	1.72	9.0	-0.17	-0.54
	64	10537.8	9798.7	-0.690±0.010	-6.6±0.6	2.04	21.5	-0.30	-0.21
	65	10272.8	9779.8	-0.344±0.012	-3.2±0.5	2.02	21.3	-0.15	0.05
	66	14570.6	14180.4	-0.028±0.007	-0.4±0.7	1.88	27.1	-0.01	3.36

67	8665.2	8067.3	-0.320±0.012	-2.5±0.2	1.76	15.5	-0.16	0.55
68	9567.2	9352.0	-0.073±0.010	-0.6±0.1	1.46	14.0	-0.05	2.19
nAP*	26325.3	25191.1	-0.463±0.006	-11.0±1.2				
nAP East*	13371.2	12921.7	-0.651±0.008	-7.8±0.6				
nAP North*	1310.8	1302.5	-0.067±0.004	-0.1±0.0				
nAP West*	11643.3	10966.8	-0.286±0.016	-3.0±0.7				
No IS[+]	28445.0	27149.4	-0.171±0.005	-4.4±1.2				
IS break[+]	58628.1	51064.4	-0.316±0.003	-16.7±2.3				
IS no break[+]	34541.7	30460.6	-0.123±0.003	-3.8±1.1				
Rott18°	11778.3	11347.7	-0.692±0.009	-7.3±0.6				

615

Table 2: Comparison of glacier mass balances obtained in this study and by Rignot et al. (2019) for the period 2013-2017. S: glacier area; ΔM/Δt: total and specific mass balance. *assumed balanced mass budget by Rignot et al. (2019), +excluding glaciers with assumed balanced mass budget

Glacier	This study			Rignot et al. (2019)			difference	
	S (km²)	$\Delta M/\Delta t$ (Gt/a)	$\Delta M/\Delta t$ (kg/m²/a)	S (km²)	$\Delta M/\Delta t$ (Gt/a)	$\Delta M/\Delta t$ (kg/m²/a)	S (%)	$\Delta M/\Delta t$ (%)
Crane	1139	-0.57±0.06	-0.50	1216	-1.11±0.18	-0.91	-6.7	83.4
Drygalski	945	-1.96±0.14	-2.07	996	-4.29±0.80	-4.31	-5.4	107.8
Flask	1137	-0.34±0.04	-0.30	1178	-0.53±0.18	-0.45	-3.6	50.8
Fleming	7710	-4.92±0.55	-0.64	8988	-8.02±2.77	-0.89	-16.6	-39.8
HGE	1401	-2.51±0.19	-1.79	1431	-7.24±0.31	-5.06	-2.1	183.0
Jorum	417	-0.13±0.03	-0.31	520	-0.21±0.06	-0.40	-24.6	28.1
Leppard	1566	-0.55±0.06	-0.35	1812	-0.30±0.22	-0.16	-15.7	-53.6
Mapple*	130	-0.03±0.01	-0.26	187	0.00±0.07	0.00	0.0	-100
Melville	187	-0.09±0.01	-0.49	281	-0.10±0.00	-0.36	-50.1	-28
Pequod*	229	-0.01±0.02	-0.06	327	0.00±0.01	0.00	-43.3	-100
Punchbowl*	108	-0.02±0.01	-0.18	99	0.00±0.01	0.00	8.3	-100
Starbuck*	253	0.01±0.01	0.03	280	0.00±0.02	0.00	-10.9	-100
Stubb*	177	-0.01±0.02	-0.07	196	0.00±0.03	0.00	-10.9	-100
Total	15399	-11.14±1.16	-0.72	17512	-21.80+ -4.66	-1.25	-13.7	72%
Total+	14503	-11.07±1.08	-0.76	16421	-21.80+ -4.53	-1.32	-13.2	74%

620